SKY CALIBRATION USING FAST HOLOGRAPHIC DECONVOLUTION

Joshua Kerrigan
joshua_kerrigan@brown.edu

Jonathan Pober
jonathan_pober@brown.edu

June 5, 2019

ABSTRACT

The Hydrogen Epoch of Reionization Array (HERA) was built to exploit the method of redundant calibration which assumes a high degree of redundancy in the layout of the array. This method however has some shortcomings such as the array not being ideally redundant and having no reference to a physical sky. We present an alternative approach using the Fast Holographic Deconvolution (FHD) interferometry software package to perform a wide-field sky calibration of HERA IDR2 observations using the extensive extragalactic point source catalog, the GaLactic and Extragalactic All-sky Mwa (GLEAM) catalog. In doing this we outline several calibration schemes that have been found to produce favorable results at the current build-out stage of HERA.

1 Sky Calibration

Calibration is the process of correcting for instrumental effects present in the array and associating it with a proper physical scaling relative to the sky. Calibration has proven to be one of the more difficult aspects of pursuing the 21cm reionization signal. This has been such a concern that many 21cm cosmology radio interferometers have been purpose built to leverage redundancy in their layout to improve calibration. The strength of redundant calibration is that no *a priori* assumptions are made concerning the sky [1, 2]. Unfortunately, this leaves the interferometer physically unrelated to the sky meaning the array is only internally consistent. Additionally, redundant calibration relies on every baseline visibility being perfectly redundant but this is typically not the case due to individual antenna characteristics. To relate the redundantly calibrated interferometer visibilities to the sky, a source catalog of extragalactic point sources must be used to fit for both an absolute amplitude and phase. The default approach for HERA is to do this with the Common Astronomy Software Applications (CASA) package and one or a few strong point sources in the sky to calibrate. This may not be optimal as many locations in the sky do not have very strong calibrators and the few locations in the southern sky that do are usually extended sources which add an additional layer of complexity to the calibration of a low spatial resolution interferometer. In addition to these limitations CASA doesn't support the use of a primary beam model. This pipeline for HERA can found at `https://github.com/HERA-Team/hera_cal` which includes redundant calibration [2, 3], CASA absolute calibration [4], and averaging of nights in LST (*aka* LST binning) [5]. We therefore look at an alternate approach for calibrating HERA observations by using the radio interferometry simulation and calibration software known as Fast Holographic Deconvolution (FHD).

2 HERA Data

The methods outlined in this memo work with raw preliminary HERA-52 data with RFI flagging performed using the legacy XRFI watershed algorithm which is the only post-processing from the Initial Data Release (IDR) 2 dataset. This means that no redundant calibration, removal of malfunctioning antennas, or handling of other array systematics has been allowed prior to handing off to FHD. We intend to use results of the FHD sky calibration process to measure and identify details such as bad data from malfunctioning antennas and array systematics. The dataset consists of observations from JD 2458098-2458116 with each daily observing period covering $1h32m \leq \mathrm{RA} \leq 10h9m$. Each 10 minute observation is split into 12 smaller observations of 50 seconds to minimize error when calibrating. Therefore

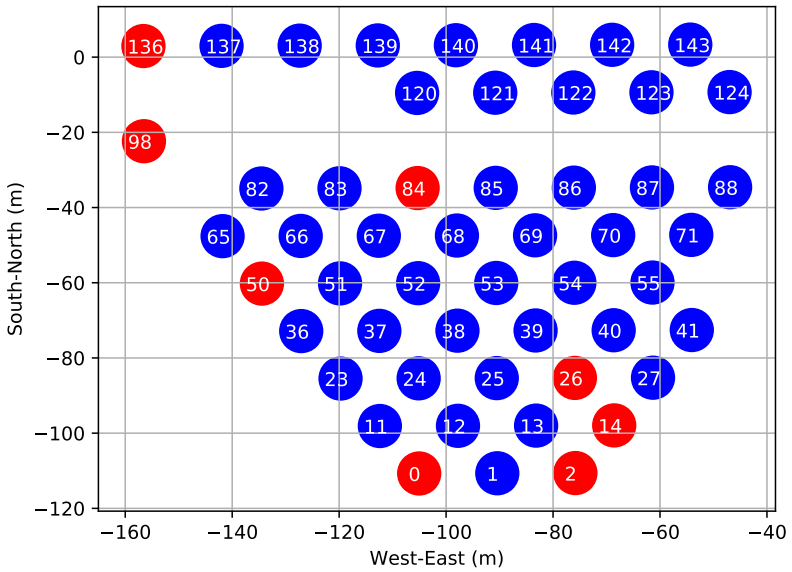

Figure 1: The antenna layout at the time the HERA-52 data was observed. Blue antennas are deemed to be suitable while red antennas are bad. Some noticeable differences between this work and [4] is that we determine antennas **11** and **121** to be stable when compared to the average of antenna calibrations and that antenna **136** is unstable (this antenna was not available at the time of the analysis presented in [4].

calibration solutions are fit per every 50 s observation per frequency channel and per antenna with no further attempt at reducing the degrees of freedom.

3 Fast Holographic Deconvolution

Fast Holographic Deconvolution[1] or FHD as it will be referred to in the remainder of this memo is a software package for simulating and calibrating radio interferometry data. It is written in IDL and driven by bash scripts for performing batch processing. Running FHD for any specific radio interferometer requires several key components a **primary beam model**, **source catalog**, **parameter script**, and **observation data**.

3.0.1 HERA Primary Beam Model

Ideally, a primary beam model should simulate both the spatial and spectral response precisely because inaccuracies in either could introduce aliasing, contamination, or leakage into the power spectrum. One such example that is a concern for low frequency EoR studies is from primary beam chromaticity[2] [6] which can introduce foreground power well into the EoR window therefore obscuring a detection. The HERA dish/antenna was purposefully designed with this element in mind and should have a reduced response to the beam chromaticity. The **beam model** supplied to FHD can be either an analytic representation that is computed on the fly (e.g. MWA Beam Model Version #2),a simple analytic model such as an Airy disk / Gaussian, or a pre-stored simulation. For this HERA-52 analysis we use a pre-stored beam model simulation[3]. The simulated beam model is from a CST EM[4] simulation that numerically solves Maxwell's equations for simulated 3D RF engineering applications. The simulated HERA primary beam model is mapped to the sky in HEALpix [7] coordinates with an NSIDE of 128 and provides the resolution of a 1 MHz/channel spectral response of a single antenna over the observing band. This spectral response is more finely sampled using a cubic interpolation down

[1]The FHD development repository can be found at `https://github.com/EoRImaging/FHD`. This analysis was performed using the FHD branch HERA with a githash of 417241627c0bdd7c1dee3fffc0820c31d2fb354f.

[2]Not to be confused with the chromaticity introduced from the frequency dependence of the measured uv-plane Fourier modes, synthesized beam.

[3]HERA RAW CST primary beam models can be found at `https://github.com/Nicolas-Fagnoni/Simulations`.

[4]CST is the Computer Simulation Technology 3D simulator for electromagnetic fields.

to a frequency resolution of 97.8 kHz/channel to match the HERA passband resolution, and is inspected to ensure there is no aliasing.

3.0.2 Source Catalog

The **source catalog** used is typically the Galactic and Extragalactic All-Sky MWA (GLEAM) catalog which contains over 300,000 unique extragalctic point sources as found by the MWA. FHD does not require any particular source catalog and user defined or created ones can be used. These catalogs are simple arrays with information such as the (RA,Dec) positioning on the sky, flux of the source, α which is the source spectral index, and the frequency the flux measurement was observed at f_0. Some acceptable versions of the GLEAM catalog for FHD include 'mwa_calibration_source_list_gleam_kgs_fhd_fornax.sav', 'GLEAM_plus_rlb2017.sav', and 'GLEAM_v2_plus_rlb2019.sav'[5]. These catalogs are all found in the **FHD/catalog_data** directory and can be accessed independently from IDL by using scipy's readsav() function. Calibration of HERA data in this memo exclusively used the 'GLEAM_plus_rlb2017.sav' catalog.

3.0.3 Parameter Script

A **parameter script** is simply the script that sets important imaging, simulation, calibration, or deconvolution settings in the underlying FHD processes. A sample of some critical parameters used by FHD for HERA-52 calibration is shown in Table 1. These parameters are instrument dependent and therefore not all parameters used for one interferometer will translate well to another.

3.0.4 Observational Data

Observational data is important if using FHD for calibration and deconvolution/foreground subtraction. This data can be in the form of raw or pre-calibrated (redundantly calibrated) visibilities but must be in the **uvfits**[6] file format. Overly flagged data due to RFI can present issues during calibration because of lack of convergence and the same goes for missed RFI which pollutes the image causing low SNR.

3.1 Capabilities

FHD can perform calibration, simulation, and imaging. The process of calibration involves the creation of model visibilities implying that for every calibration you are also performing a simulation. If foreground subtraction is performed FHD can calibrate the data against a source catalog that it will simulate model visibilities for providing an output of calibrated observed, model, and residual visibilities. Residual in this case means the subtraction of the model visibilities from the calibrated observed visibilities and is typically referred to as foreground subtraction.

3.2 Under the hood

FHD relative to other radio interferometer simulators such as PRISim[7] [8] and pyuvsim[8] [9] is fast but potentially trades off precision for that speed. This speed increase is directly attributed to the holographic mapping formulation

$$\mathbf{H}(\mathbf{u},\mathbf{u}) = \tilde{\mathbf{B}}^{\mathbf{T}}(\mathbf{u},\mathbf{V})\mathbf{B}(\mathbf{V},\mathbf{u})\,, \tag{1}$$

which reduces computational time by directly mapping the model visibilities $\mathbf{B}(\mathbf{V},\mathbf{u})$ and holographic antenna beams $\tilde{\mathbf{B}}^{\mathbf{T}}(\mathbf{u},\mathbf{V})$ from their locations in the model uv plane $\mathbf{u}$ to their position in the holographic map of visibilities $\mathbf{V}$ i.e. $\mathbf{V} \leftrightarrow \mathbf{u}$ [10]. This is in contrast to the need for other simulators to integrate across the uv-plane to create model visibilities which is very time consuming. The holographic mapping function $\mathbf{H}(\mathbf{u},\mathbf{u})$ is computed for each observation and polarization.

For calibration FHD performs a least squares regression on the χ^2 equation

$$\chi^2 = \sum_{ij} \frac{|v_{ij} - g_i g_j^* m_{ij}|^2}{\sigma_{ij}^2}\,, \tag{2}$$

[5]Credit to Ruby Byrne for compiling the GLEAM+ catalogs which consist of the standard GLEAM components in addition to several extended and point sources.

[6]pyuvdata can be used for converting between filetypes such as Miriad, uvfits, and measurement sets. It can be found at `https://github.com/RadioAstronomySoftwareGroup/pyuvdata`

[7]`https://github.com/nithyanandan/PRISim`

[8]`https://github.com/RadioAstronomySoftwareGroup/pyuvsim`

where m_{ij} is the FHD generated model visibility, g_i the gain from the ith antenna, v_{ij} the raw visibility which contains noise, σ_{ij} the noise variance of the i, j baseline visibility and $*$ represents the complex conjugate. This is solved per frequency channel and per polarization. By default FHD solves for an average calibration across all times which can be problematic if the sky transits substantially over an observation, which for a standard 10 minute HERA observation gives a difference of $\delta\theta = 2.5^\circ$ between the initial and final time integrations. Applying these time-averaged calibrations over all integrations would introduce increasing amplitude and phase errors approaching both ends of the observation. This is accounted for in this work by slicing HERA-52 observations into smaller 50 s ($\delta\theta = 12.5'$) observations, down from their typical 10 minute totals. Doing this should reduce any time dependent calibration errors down by a factor of ~ 5 provided the center RA of the observation is used for calibration.

In this analysis we look at only the XX[9] polarization, because while the YY polarization beam model is nearly identical to the XX beam model up to a 90° rotation this was not properly performed in the primary beam model on hand. In the default calibration pipeline for the Murchison Widefield Array (MWA), smoothing is performed independently on amplitude and phase with a low order polynomial using the FHD keywords cal_amp_degree_fit and cal_phase_degree_fit, with the amplitude order being set to 2 and phase order set to 1. We do not perform any smoothing of the calibration solutions in this memo. However, if we were to smooth the calibration solutions for HERA, a significant increase in the amplitude degree would be required due to the more complex nature of the HERA passband. In that instance, a polynomial of $\mathcal{O}(p) \geq 5$ has been found to be sufficient.

3.3 Caveats

FHD has been proven to have issues in the past, most notably pointed out in [11]), where Precision Array for Probing the Epoch of Reionization (PAPER) observations were modeled in FHD. The resulting model visibilities had issues at high-delay modes (into the EoR window) where aliasing due to uv-gridding causes these errors to be transferred to the residual foreground subtracted observations. This high delay aliasing can be reduced with increased sampling rates of the uv-plane. However it becomes extremely costly computationally. Unfortunately these high-delay modeling errors still persist for HERA (see Figure 2).

Therefore as of now there are only two relevant solutions that exist without dealing with this directly within the FHD code. One is to filter out high delays in the model visibilities as was performed in [11], removing this aliasing which in turn also removes a good deal of the beam main- and side-lobe leakage that we'd like to mitigate in the first place. The other is calibrating an entire observing night of HERA observations using an extremely fine uv-plane resolution to reduce the aliasing and then transfer the model and calibration solutions to every other observing night. The latter is of course the more appropriate solution as it still allows for capturing and correcting of the beam leakage into the EoR Window as long as the high delay calibration errors can be reduced to a sub-EoR level. Obtaining a more accurate beam model is more important before this effect becomes relevant. At this stage we do not perform either of these solutions as there is a more pressing issue of understanding the instrument calibration and reliability.

An additional caveat includes the inability to currently use diffuse maps for calibration or subtraction; this is due to both not having precise diffuse catalogs and a not entirely fleshed out diffuse modeling code infrastructure. A first attempt at integrating a diffuse map for calibration could potentially be made by using the [12] GSM diffuse sky map or the newer more high resolution GSM from [13]. These diffuse sky maps do pose some conflicts if being used in conjunction with the previously mentioned GLEAM and modified GLEAM point source catalogs, because the diffuse maps also include extended sources such as Fornax A. If calibrating off a complete diffuse + point source sky there will be significant flux over-counting and therefore either these extended sources need to be pruned from the point source catalog or regions of the sky need to be avoided. As of writing this memo however these features are still intended to be developed as options for FHD and will be included in future versions.

4 Sky Calibration

4.1 Runtime

The runtime for FHD calibration on a single sliced (5 time integrations by 1024 frequency channels) HERA observation using the parameters from Table 1 on the resources of 2 cpus with 20 GB of memory is ~ 30 minutes. This runtime is highly dependent on the FHD parameters. The key parameters are the FoV and dimension which implicitly set the resolution and dimension of the uv plane which dramatically increases memory requirements for more dense uv plane samplings.

[9] FHD uses the XX, YY polarization convention in contrast to the convention adopted by the HERA collaboration which uses E for XX and N for YY.

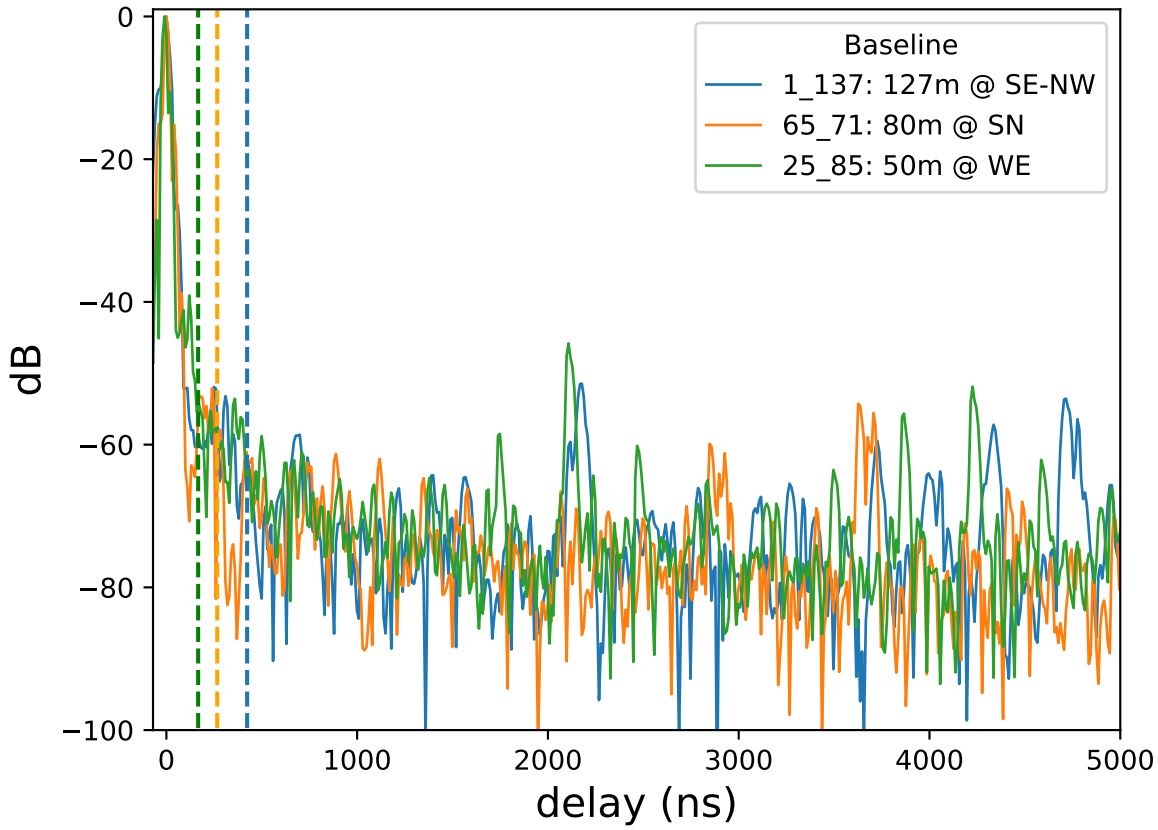

Figure 2: FHD simulated model delay spectra demonstrating the aliasing errors from the uv gridding process for several baseline lengths at different orientations. The vertical dashed lines represent the horizon limit for each baseline type. As per [11], to drive down this high delay aliasing 'noise' the uv-plane gridding resolution must be significantly increased but this has the considerable trade-off of more demanding computational needs. The uv-plane gridding resolution used here is 1.27 λ.

4.2 Calibration Case Studies

To gain an understanding of how well we are calibrating the observations we use two distinct cases. In the extreme case we look to an observation containing the extended extragalactic source of Fornax A (RA 3h 22m). For the more mild case we use the case study from [4] (RA 2h 00m) which contains two bright point sources at the center of the beam. Additional concerns that we cannot and do not attempt to control for in these two instances is diffuse emission and polarization. While these issues are not the primary concern for this work they do require a more in-depth exploration such as was covered in [14] and [15]. The FHD calibration software does have the ability to perform calibration using data from all 4 polarizations (XX, YY, XY, YX) provided the correct E-field beam is used.

To find appropriate parameters for calibrating this dataset using FHD, a coarse grid search was performed by calibrating a small sample of observations and looking at the ratio of the visibility amplitudes between the residual V_{res}, and the dirty V_{dirty}. An ideal calibration should result in a net decrease of power on the sky as sources are removed. An example of one of these grid searches is shown in Figure 3, where the relationship between how a minimum baseline cutoff affects the residuals across baseline length $|\vec{u}|$.

4.2.1 Fornax A: Bright Extended Off Zenith Source

In this section we try to understand how a bright extended source that is off zenith affects the calibration results. We approach this by looking at how we model Fornax A as either a many component extended source, or a single point

Parameter	**Values** (units)	**Definition**
FoV	45 (°)	Field of view, directly sets the extent in uv-space
dimension	1024 (px)	Dimension of the image in pixels
instrument	hera	Important for initializing several array dependent properties (e.g. beam model)
freq_start	110 (MHz)	Low end bandpass cutoff
freq_end	190 (MHz)	High end bandpass cutoff
nfreq_avg	1	Rate of frequency channel averaging
n_pol	2	Number of polarizations to calibrate (4 pol would include XX,YY,XY,YX)
calibrate_visibilities	1	Allow FHD to calibrate visibility data
flag_calibration	1	Allow FHD to flag poor calibrations
calibration_polyfit	0	Apply a polynomial fit to the amplitude and phase solutions
bandpass_calibrate	0	Apply a global bandpass fit to antennas
firstpass	1	Calibrate and subtract data using premade source catalogs
min_baseline	0 (λ)	Minimum baseline to simulate and image
min_cal_baseline	25 (λ)	Minimum baseline to use during calibration

Table 1: FHD parameters for calibrating HERA-52 data. These parameters have been determined by maximizing the amount of power removed from the visibilities during foreground subtraction, implying that a proper calibration should result in correspondence to the model visibilities simulated by FHD.

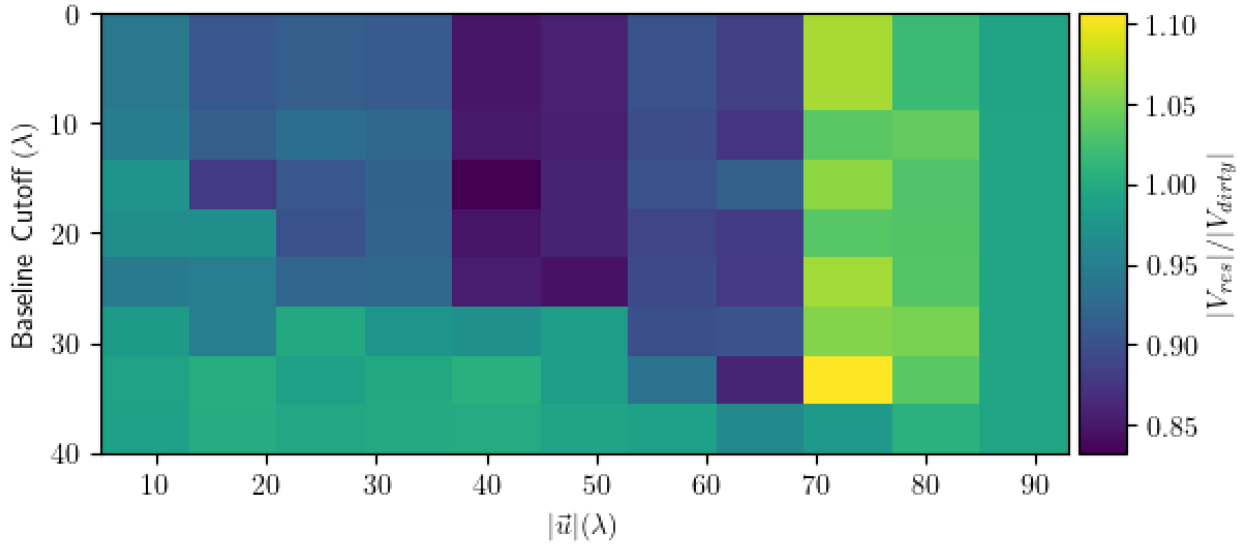

Figure 3: Average ratio of dirty V_{dirty} and residual V_{res} visibilities across baselines as a function of calibrating with a baseline cutoff.

source and additionally how it affects the calibration as it moves in and out of the sidelobes. In this analysis it is important to note that the HERA beam model is relatively untrustworthy below 10% of its maximum. This is a problem in all cases but is more important here because Fornax A never transits through the beam center and will spend the majority of its time within the poorly modeled portion of the main lobe and will remain a continued nuisance well into the beam's sidelobes. Due to the longest baseline $b_{\max} = 92\lambda$ in this HERA-52 dataset giving an angular resolution of $\delta\theta = 37.4'$ at 150 MHz, HERA-52 is right at the edge of being able to resolve Fornax A which has an angular size (radio lobe-to-lobe) of $\sim 60'$. This means that an extended source model for Fornax A (shown in Figure 5) should be used. Indeed when attempting to run this exact same calibration scheme but with Fornax A modeled as a point source (flux summed into a single component) the results are poor with a residual image that has substantial over-subtraction of Fornax A and its sidelobes. The Dirty, Model, and Residual sky images of Fornax A are shown in Figure 4. As Fornax A is the brightest extragalactic source in HERA's observing field, artifacts from malfunctioning antennae, a poor primary beam model, phase errors, dipole-arm leakage, or source position errors should worsen the calibration and final sky image. Looking at the residual image there are two mis-subtractions located at $(-28°, 50°)$ and $(-21°, 41°)$ which are left over from the sidelobes of Fornax A. Incorrect modeling of Fornax A in this instance could suggest it's a primary beam model issue because if the source model was incorrect we should see mis-subtraction doubles (positive and negative source residuals) in more locations.

4.2.2 GLEAM J0200-3053: Point Source

For a comparison to the absolute calibration work performed by [4] we look at the exact same case of point source J0200-3053 where zenith of the observation is RA 2h 00m 12.7s. This source is ideal as a calibrator in comparison to Fornax A because it is approximately a point source and transits directly through the peak of the primary beam, where beam model errors should be minimal. Looking to Figure 6 the dirty, model, and residual sky images are shown and at first glance the dirty and model appear to be in agreement. Compared to the Fornax A case both of the sources near zenith appear accounted for in the main lobe of the primary beam. The flux density remaining at the first sidelobes of the primary beam however are somewhat expected as the reliability of the HERA primary beam model at those levels is questionable.

5 HERA-52 Calibration Stability

5.1 Per Day Calibration Solution Waterfalls

The HERA-52 dataset consists of 18 nights of observation and to get an idea of how stable the array is night to night we can look to the calibration solutions over all nights and LSTs. A waterfall sampling of antenna 53's gain amplitude calibration solutions across all frequency channels (1024) and from $1.5 < t < 11.5$ h LST are shown in Figure 7. Two features that stick out are the large gain amplitudes (dark purple) centered at ~ 8 h LST and the contrast in the gain drop from Fornax A at 3.2 h LST. The feature at 8 h LST is from the sky model deteriorating as the GLEAM catalog loses point sources to the Galactic plane which causes the calibration to try and account for power in the sky that is in the raw visibilities but is not in the model visibilities. The sharp drop in the gains during the Fornax A transit is less obvious however but points heavily to poorly modeled beam sidelobes. The sudden decrease in gain amplitude is more easily seen in Figure 8, where slices through LST over the frequency channels of 130 MHz (red) and 160 MHz (black) demonstrate the time variability of calibration solutions. The double trough of the gain drop between $2.5 < t < 3.5$ h appears to peak at the beam midpoint in RA as Fornax A goes between off-center RA and DECs.

Generally speaking, antenna 53 over the course of the 18 observing nights appears to be quite stable. The night-to-night gain calibrations are within $\sim 2\%$ of the initial observing JD with little to negligible drift if any at all. To extrapolate this finding to the broader array we can compare the calibration solutions of antenna 53 to the remaining antennae in the array.

5.2 Per Antenna Correlation

To demonstrate the degree to which calibration amplitude solutions vary between antenna to antenna we form a correlation matrix in Figure 9 of the gains $|g(\nu)_i|$ from antenna i with the gains $|g(\nu)_j|$ from antenna j. Therefore each (i, j) pixel is the correlation coefficient of

$$R_{i,j} = \frac{C_{i,j}}{\sqrt{C_{i,i} * C_{j,j}}}\,, \tag{3}$$

where $C_{i,j} = \mathrm{cov}(|g(\nu)_i|, |g(\nu)_j|)$. We must take additional care when building these correlations as the discontinuities introduced by RFI flagging produce stronger correlations between antennae than we should expect and we therefore mask this missing data. Looking at Figure 9 we can see that there are two classes of broadband gain amplitude solutions

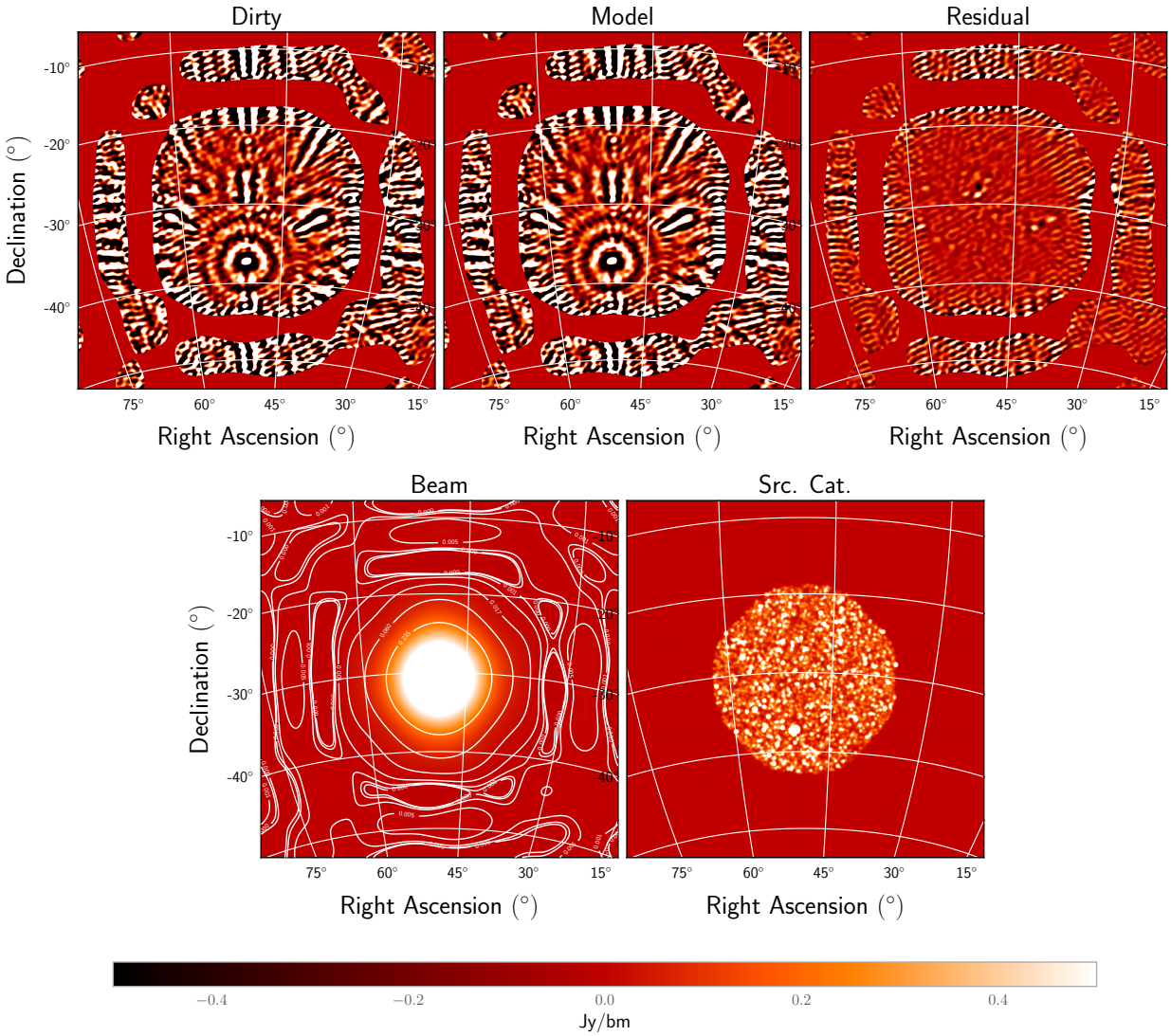

Figure 4: Observing JD 2458098 of Fornax A as Multi-Frequency Synthesis (MFS) imaged with HERA-52 and calibrated using FHD with the GLEAM source catalog. The calibration and subtraction parameters used for these images were the same as used from §1. In this case Fornax A is modeled as several individual components ($N_{\mathrm{comps}} = 1925$) as opposed to a single approximate point source; an example of this extended source model can be seen in Figure 5. An indication that the beam model is not correct can be seen in the mis-subtraction of Fornax A's sidelobes.

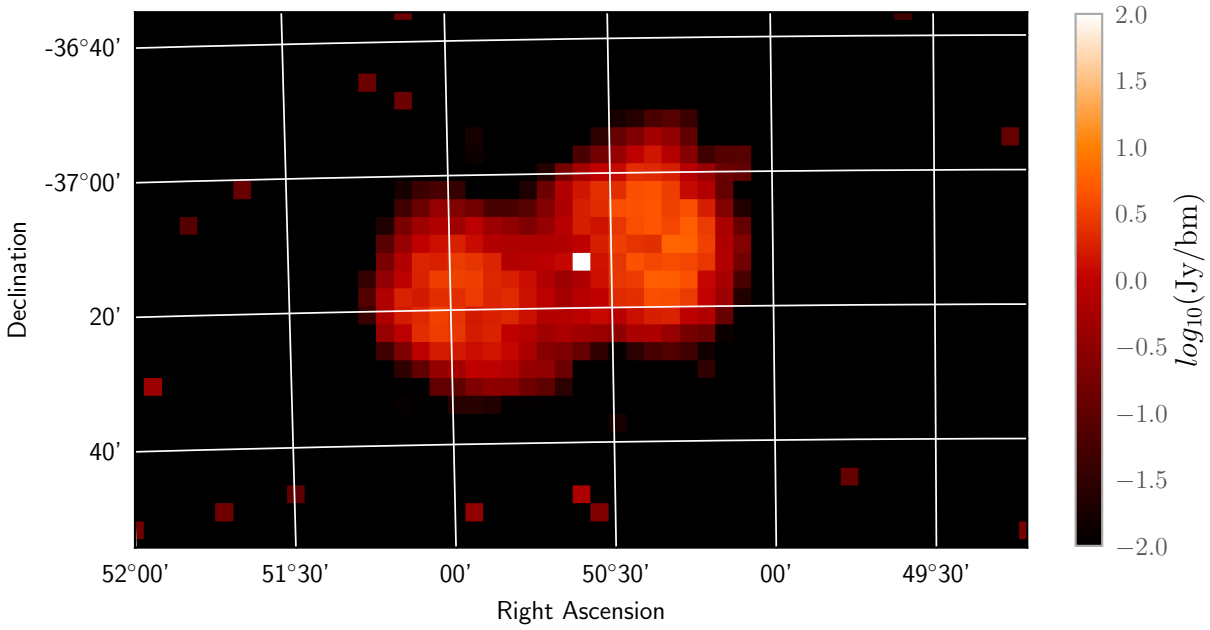

Figure 5: The extended source GLEAM model used for Fornax A at 150 MHz with a peak flux of $\sim$ 313 Jy. A total of 1925 components are used for this model.

between antenna pairs. The two distinct modes can be seen in the passband gain solutions in Figure 10 and appear to be linked to the difference in front-end modules used. For reference, front-end modules here contain a series of Low Noise Amplifiers (LNAs) which are then attached to a hybrid coupler (balun) and should be impedance matched [16] with the output signal path to reduce ripples in the passband. Antenna's having a front-end with a nomenclature of 'FEA' are **51, 65, 66, 70, 82, 83, 98, 120, 121, 122, 123, 124, 141, 142, 143** and correspond to the blue curves from Figure 10. Using both Figure 9 and Figure 10 the degree to which the broader array and the intra-mode correspondence can be approximated. The average antenna to antenna intra-mode variation for the passband across mode 1 is $< 9\%$ and for mode 2 is $< 12\%$. According to the correlation matrix antenna **67** is behaving uniquely in so much that it does not fit either of the two modes identified. Also interesting is that while antenna **142** has a front-end 'FEA' module and should be within the secondary mode, it corresponds more closely to the first mode implying that its passband ripples may not be as attenuated. If both antenna **67** and **142** are removed the intra-mode variation for mode 1 reduces to $< 7\%$.

6 Calibration Results

I find that overall the preliminary HERA-52 dataset and array is nominally stable over the 18 nights of observation. However, several precautions should be taken for the purpose of performing any type of power spectrum analysis such as removal of antenna **67**, and **142** as they both seem to be exhibiting behavior outside the two operating modes. For cuts along observing night, JD 2458104 and 2458109 should be excluded as they appear to have some time stamp issues and don't align time-wise with the rest of the observing nights. Based on the calibration of these 18 nights the average variation across the array and bandpass is $\sim 10\%$, with the night-to-night variation being $\sim 2\%$. Looking to the FHD sky calibrated waterfall visibilities in Figure 11, there is close agreement with the FHD model to the observed data. Baseline '13_25' displays fairly close to the same amount of power post-subtraction due to the calibration baseline length threshold set in the initial parameters and also because diffuse emissions are stronger in short baselines. Residual power seen in the mid and long baselines see a substantial amount of foreground power removal. The longer baseline waterfall visibilities where power was left behind in the wake of Fornax A's removal could very well be due to the HERA primary beam model's spectral response being insufficiently modeled or possibly the requirement for an even higher fidelity Fornax A model. In either case an improved HERA primary beam model will be needed as its limitations

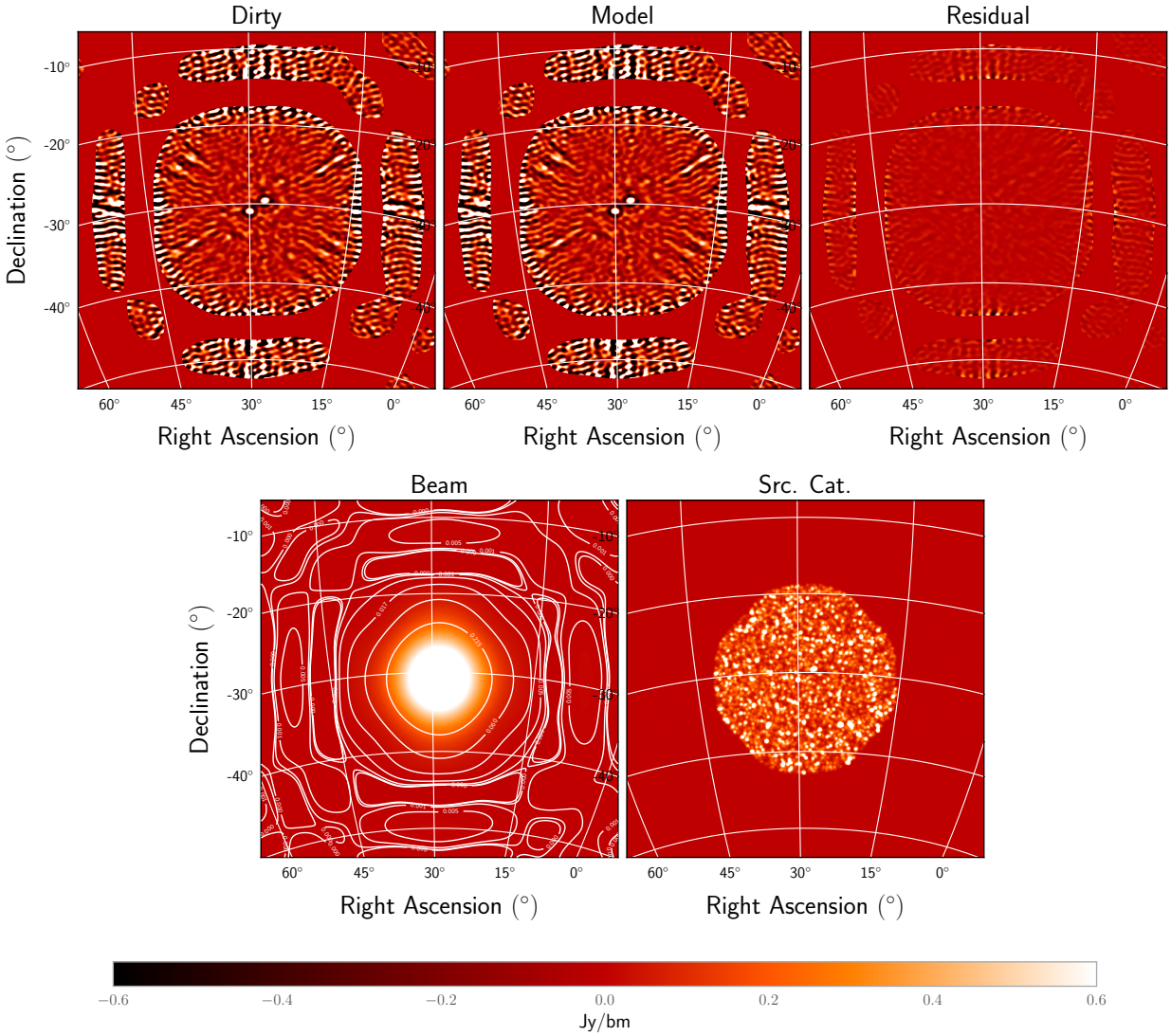

Figure 6: The same field as covered in [4] which used GLEAM J0200-3053 as a primary calibrator. In this example we attempt to calibrate using an entire field of sources (N_{sources} = 8238) all located within 10% of the beam max. We can see that with sources that are much better approximations to point sources and are located beam center we have significant improvements in the Residual image for both the main- and side- lobes.

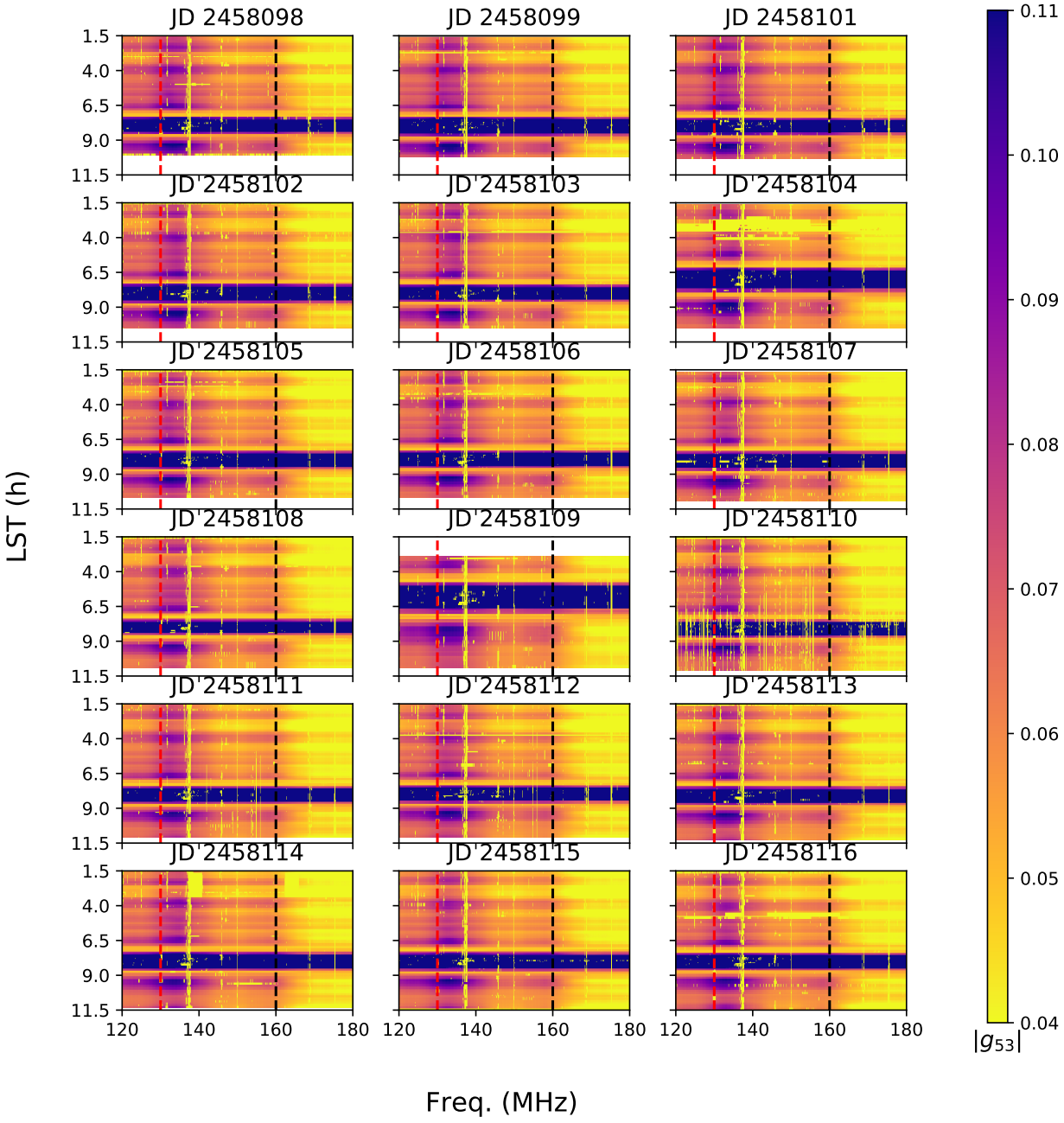

Figure 7: The per observing night gain calibration amplitudes for antenna 53. The regions of missing gains are from RFI removal performed prior to calibrating in FHD. The bright(dark purple) broad feature in the gain amplitudes is due to FHD attempting to account for power on the sky from our own galaxy which GLEAM does not provide sources for resulting in meaningless amplitude solutions. The vertical dashed red and black lines correspond to slices taken in frequency and shown in Figure 8

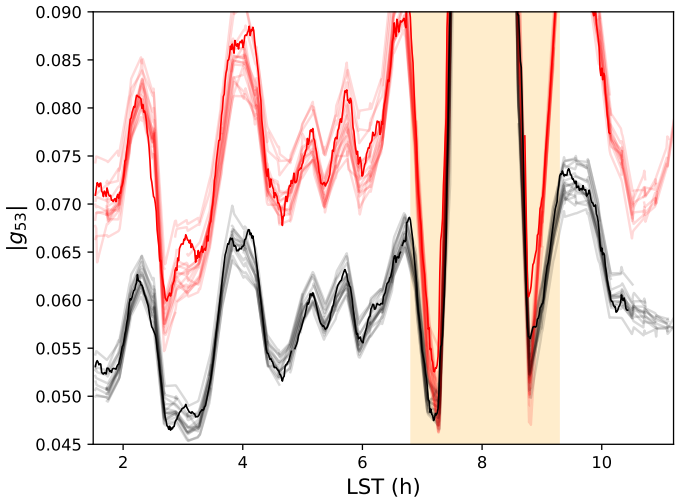

Figure 8: Gain amplitude slices for antenna 53 over LST at center frequencies of 130 MHz (red) and 160 MHz (black) demonstrating the time dependent structure from calibration. Gains were sampled roughly every 10 minutes for the background ensemble of calibrations that have reduced opacity. The opaque red and black lines are more finely sampled at 10 second intervals from JD 2458101 to give a better idea of the structure over LST. The dip seen centered at ~ 3.4 hrs is when Fornax A is at zenith. The orange shaded region represents the incomplete sky catalog due to the Milky Way.

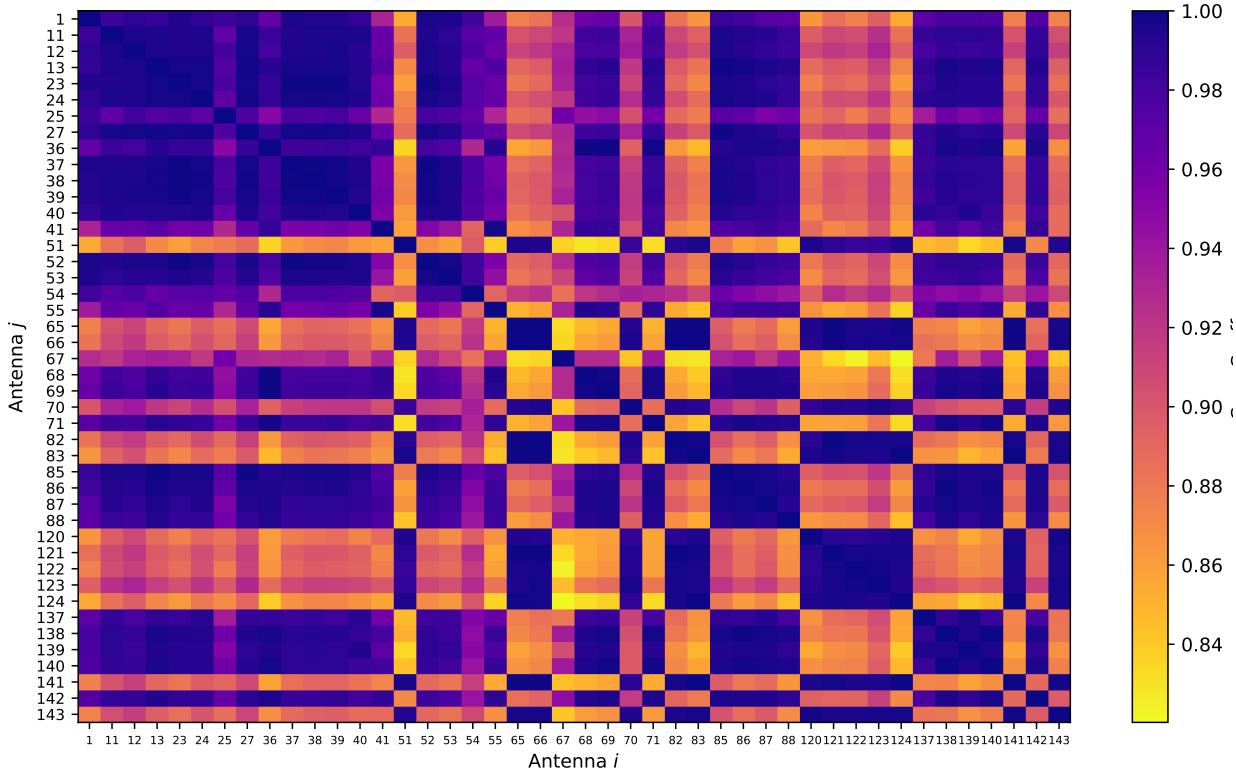

Figure 9: The correlation matrix between all antennas that were deemed functional from JD 2458101 at 2.36h LST. The two antenna modes can be easily distinguished here as their per frequency gain amplitude solutions do not correlate particularly well with one another.

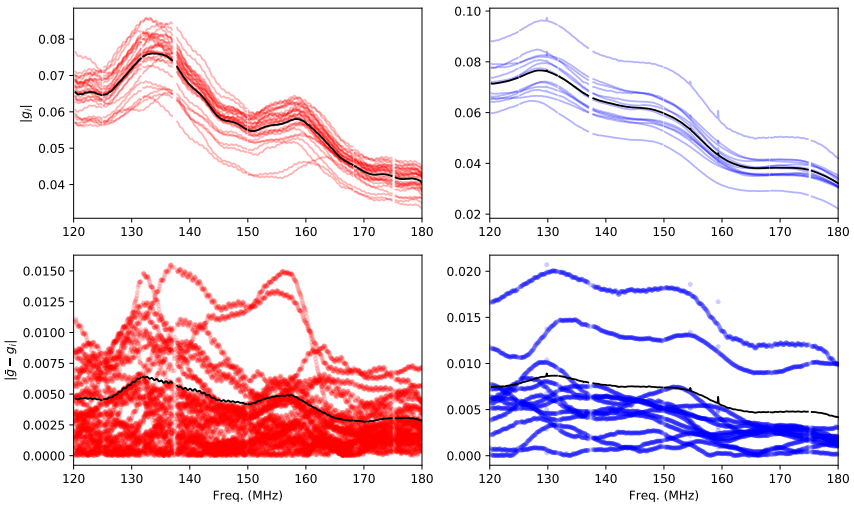

Figure 10: Plots demonstrating the two distinct modes (left and right columns) seen in the HERA-52 dataset. The bottom two figures show the difference between each antenna's gains g_i and the mode group average $\bar{g}_i$. The black curves represent the average of antennas per mode per frequency (top) and the standard deviation per antenna mode per frequency (bottom).

are still apparent from Figure 8 where calibration gain amplitudes attempt to account for bright sources away from beam center and down into the sidelobes.

7 Conclusion

The calibration pipeline and analysis presented here offers an additional avenue for validating the default HERA redundant and absolute calibration pipeline. Recent efforts have been made to explore the limitations of both sky calibration [17] and redundant calibration [18], which places more emphasis on being aware of the bias inherent in either calibration procedure. A common theme for limiting the precision of these calibrations stems from an incomplete sky model. While the GLEAM catalog is an amazing resource for extragalactic point sources as of right now, the inclusion of a diffuse sky model native to the EoR observing band could lead to a significant leap in calibration results. A proper diffuse sky catalog is however left to a future endeavor as there are more immediate needs for the development of HERA. For example a simulated complex E-field primary beam would give FHD the ability to calculate the full proper Jones matrices and calibrate across polarizations to account for polarization leakage [19, 20, 14]. This is a project that is being worked on as of writing this memo, with the results of this work being a perfect comparison for any proceeding HERA calibration performed with a complex E-field beam.

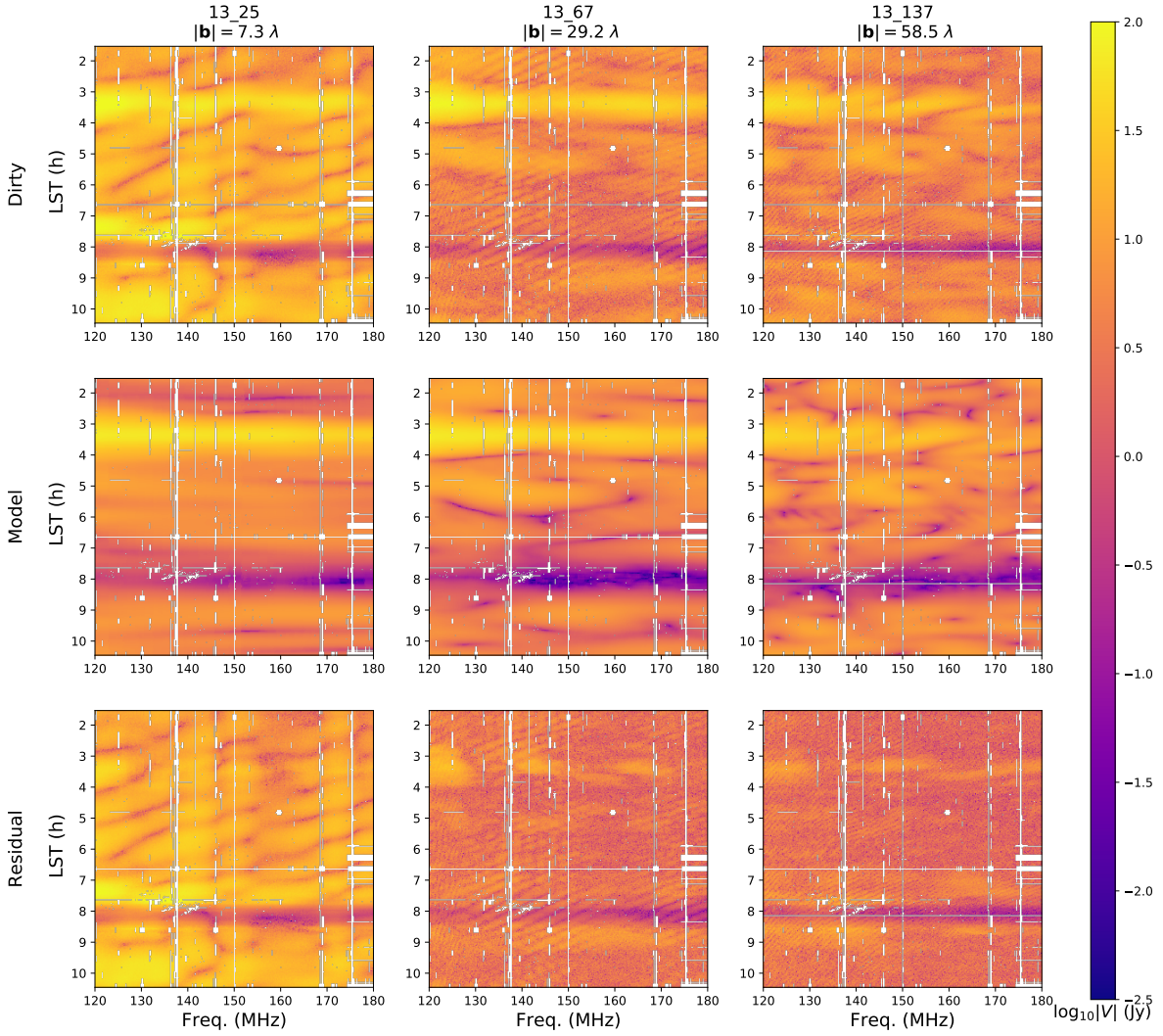

Figure 11: Waterfall visibilities of the FHD calibrated HERA data (top row), Model (middle row), and Residual (bottom row) for baselines (13,25) (shortest), (13,67), and (13,137) (longest). As should be expected, baseline (13,25) has the most power due to galactic diffuse emission and also minimal foreground mitigation in the residual waterfall visibilities. Baselines (13,67) and (13,137) were included in the calibration process while (13,25) was not due to the minimum baseline threshold of 25λ as we don't want to attempt a calibration of the shortest baselines without a diffuse sky model. Missing data (white) is due to RFI flagging.

References

[1] Adrian Liu, Max Tegmark, Scott Morrison, Andrew Lutomirski, and Matias Zaldarriaga. Precision calibration of radio interferometers using redundant baselines. , 408(2):1029–1050, Oct 2010.

[2] H. Zheng, M. Tegmark, V. Buza, J. S. Dillon, H. Gharibyan, J. Hickish, E. Kunz, A. Liu, J. Losh, A. Lutomirski, S. Morrison, S. Narayanan, A. Perko, D. Rosner, N. Sanchez, K. Schutz, S. M. Tribiano, M. Valdez, H. Yang, K. Z. Adami, I. Zelko, K. Zheng, R. P. Armstrong, R. F. Bradley, M. R. Dexter, A. Ewall-Wice, A. Magro, M. Matejek, E. Morgan, A. R. Neben, Q. Pan, R. F. Penna, C. M. Peterson, M. Su, J. Villasenor, C. L. Williams, and Y. Zhu. MITEoR: a scalable interferometer for precision 21 cm cosmology. , 445:1084–1103, December 2014.

[3] A. Liu, A. R. Parsons, and C. M. Trott. Epoch of reionization window. II. Statistical methods for foreground wedge reduction. , 90(2):023019, July 2014.

[4] Kern, N., Gianni, B., and Carilli, C. ABSOLUTE CALIBRATION OF HERA-47 IDR1. *Memo Series 42, HERA Collaboration*, January 2018.

[5] Zaki S. Ali, Aaron R. Parsons, Haoxuan Zheng, Jonathan C. Pober, Adrian Liu, James E. Aguirre, Richard F. Bradley, Gianni Bernardi, Chris L. Carilli, Carina Cheng, David R. DeBoer, Matthew R. Dexter, Jasper Grobbelaar, Jasper Horrell, Daniel C. Jacobs, Pat Klima, David H. E. MacMahon, Matthys Maree, David F. Moore, Nima Razavi, Irina I. Stefan, William P. Walbrugh, and Andre Walker. Paper-64 constraints on reionization: The 21 cm power spectrum at z = 8.4. , 809(1):61, 2015.

[6] N. Thyagarajan, A. R. Parsons, D. R. DeBoer, J. D. Bowman, A. M. Ewall-Wice, A. R. Neben, and N. Patra. Effects of Antenna Beam Chromaticity on Redshifted 21 cm Power Spectrum and Implications for Hydrogen Epoch of Reionization Array. , 825:9, July 2016.

[7] K. M. Górski, E. Hivon, A. J. Banday, B. D. Wandelt, F. K. Hansen, M. Reinecke, and M. Bartelmann. HEALPix: A Framework for High-Resolution Discretization and Fast Analysis of Data Distributed on the Sphere. , 622:759–771, April 2005.

[8] N. Thyagarajan, D. C. Jacobs, J. D. Bowman, N. Barry, A. P. Beardsley, G. Bernardi, F. Briggs, R. J. Cappallo, P. Carroll, B. E. Corey, A. de Oliveira-Costa, J. S. Dillon, D. Emrich, A. Ewall-Wice, L. Feng, R. Goeke, L. J. Greenhill, B. J. Hazelton, J. N. Hewitt, N. Hurley-Walker, M. Johnston-Hollitt, D. L. Kaplan, J. C. Kasper, H.-S. Kim, P. Kittiwisit, E. Kratzenberg, E. Lenc, J. Line, A. Loeb, C. J. Lonsdale, M. J. Lynch, B. McKinley, S. R. McWhirter, D. A. Mitchell, M. F. Morales, E. Morgan, A. R. Neben, D. Oberoi, A. R. Offringa, S. M. Ord, S. Paul, B. Pindor, J. C. Pober, T. Prabu, P. Procopio, J. Riding, A. E. E. Rogers, A. Roshi, N. Udaya Shankar, S. K. Sethi, K. S. Srivani, R. Subrahmanyan, I. S. Sullivan, M. Tegmark, S. J. Tingay, C. M. Trott, M. Waterson, R. B. Wayth, R. L. Webster, A. R. Whitney, A. Williams, C. L. Williams, C. Wu, and J. S. B. Wyithe. Foregrounds in Wide-field Redshifted 21 cm Power Spectra. , 804:14, May 2015.

[9] Hazelton B. Jacobs D. Kolopanis M. Pober J. Aguirre J. Lanman, A. and T. Nithyanandan. pyuvsim: A comprehensive simulation package for radio interferometers in python. *JOSS*, May 2019.

[10] I. S. Sullivan, M. F. Morales, B. J. Hazelton, W. Arcus, D. Barnes, G. Bernardi, F. H. Briggs, J. D. Bowman, J. D. Bunton, R. J. Cappallo, B. E. Corey, A. Deshpande, L. deSouza, D. Emrich, B. M. Gaensler, R. Goeke, L. J. Greenhill, D. Herne, J. N. Hewitt, M. Johnston-Hollitt, D. L. Kaplan, J. C. Kasper, B. B. Kincaid, R. Koenig, E. Kratzenberg, C. J. Lonsdale, M. J. Lynch, S. R. McWhirter, D. A. Mitchell, E. Morgan, D. Oberoi, S. M. Ord, J. Pathikulangara, T. Prabu, R. A. Remillard, A. E. E. Rogers, A. Roshi, J. E. Salah, R. J. Sault, N. Udaya Shankar, K. S. Srivani, J. Stevens, R. Subrahmanyan, S. J. Tingay, R. B. Wayth, M. Waterson, R. L. Webster, A. R. Whitney, A. Williams, C. L. Williams, and J. S. B. Wyithe. Fast Holographic Deconvolution: A New Technique for Precision Radio Interferometry. , 759:17, November 2012.

[11] J. R. Kerrigan, J. C. Pober, Z. S. Ali, C. Cheng, A. P. Beardsley, A. R. Parsons, J. E. Aguirre, N. Barry, R. F. Bradley, G. Bernardi, C. L. Carilli, D. R. DeBoer, J. S. Dillon, D. C. Jacobs, S. A. Kohn, M. Kolopanis, A. Lanman, W. Li, A. Liu, and I. Sullivan. Improved 21 cm Epoch of Reionization Power Spectrum Measurements with a Hybrid Foreground Subtraction and Avoidance Technique. , 864:131, September 2018.

[12] A. de Oliveira-Costa, M. Tegmark, B. M. Gaensler, J. Jonas, T. L. Landecker, and P. Reich. A model of diffuse Galactic radio emission from 10 MHz to 100 GHz. , 388:247–260, July 2008.

[13] H. Zheng, M. Tegmark, J. S. Dillon, D. A. Kim, A. Liu, A. R. Neben, J. Jonas, P. Reich, and W. Reich. An improved model of diffuse galactic radio emission from 10 MHz to 5 THz. , 464(3):3486–3497, Jan 2017.

[14] S. Kohn, P. M. Chichura, A. S. Igarashi, A. F. Fortino, J. E. Aguirre, R. K. Benefo, T. S. Billings, S. Gallardo, P. La Plante, Z. E. Martinot, C. D. Nunhokee, P. Alexander, Z. S. Ali, A. P. Beardsley, G. Bernardi, J. D. Bowman, R. F. Bradley, C. L. Carilli, C. Cheng, D. R. DeBoer, E. de Lera Acedo, J. S. Dillon, A. Ewall-Wice, G. Fadana,

N. Fagnoni, R. Fritz, S. R. Furlanetto, B. Glendenning, B. Greig, J. Grobbelaar, B. J. Hazelton, J. N. Hewitt, J. Hickish, D. C. Jacobs, A. Julius, M. Kariseb, N. S. Kern, M. Kolopanis, T. Lekalake, A. Liu, A. Loots, D. MacMahon, L. Malan, C. Malgas, M. Maree, N. Mathison, E. Matsetela, A. Mesinger, M. F. Morales, A. R. Neben, B. Nikolic, A. R. Parsons, N. Patra, S. Pieterse, J. C. Pober, N. Razavi-Ghods, J. Ringuette, J. Robnett, K. Rosie, R. Sell, C. Smith, A. Syce, M. Tegmark, N. Thyagarajan, P. K. G. Williams, and H. Zheng. Polarized Foreground Power Spectra from the HERA-19 Commissioning Array. *arXiv e-prints*, February 2018.

[15] J. S. Dillon, S. A. Kohn, A. R. Parsons, J. E. Aguirre, Z. S. Ali, G. Bernardi, N. S. Kern, W. Li, A. Liu, C. D. Nunhokee, and J. C. Pober. Polarized redundant-baseline calibration for 21 cm cosmology without adding spectral structure. , 477:5670–5681, July 2018.

[16] David R. DeBoer, Aaron R. Parsons, James E. Aguirre, Paul Alexander, Zaki S. Ali, Adam P. Beardsley, Gianni Bernardi, Judd D. Bowman, Richard F. Bradley, Chris L. Carilli, Carina Cheng, Eloy de Lera Acedo, Joshua S. Dillon, Aaron Ewall-Wice, Gcobisa Fadana, Nicolas Fagnoni, Randall Fritz, Steve R. Furlanetto, Brian Glendenning, Bradley Greig, Jasper Grobbelaar, Bryna J. Hazelton, Jacqueline N. Hewitt, Jack Hickish, Daniel C. Jacobs, Austin Julius, MacCalvin Kariseb, Saul A. Kohn, Telalo Lekalake, Adrian Liu, Anita Loots, David MacMahon, Lourence Malan, Cresshim Malgas, Matthys Maree, Zachary Martinot, Nathan Mathison, Eunice Matsetela, Andrei Mesinger, Miguel F. Morales, Abraham R. Neben, Nipanjana Patra, Samantha Pieterse, Jonathan C. Pober, Nima Razavi-Ghods, Jon Ringuette, James Robnett, Kathryn Rosie, Raddwine Sell, Craig Smith, Angelo Syce, Max Tegmark, Nithyanandan Thyagarajan, Peter K. G. Williams, and Haoxuan Zheng. Hydrogen Epoch of Reionization Array (HERA). , 129(974):045001, Apr 2017.

[17] N. Barry, B. Hazelton, I. Sullivan, M. F. Morales, and J. C. Pober. Calibration requirements for detecting the 21 cm epoch of reionization power spectrum and implications for the SKA. , 461:3135–3144, September 2016.

[18] Ruby Byrne, Miguel F. Morales, Bryna Hazelton, Wenyang Li, Nichole Barry, Adam P. Beardsley, Ronniy Joseph, Jonathan Pober, Ian Sullivan, and Cathryn Trott. Fundamental Limitations on the Calibration of Redundant 21 cm Cosmology Instruments and Implications for HERA and the SKA. , 875(1):70, Apr 2019.

[19] T. D. Carozzi and G. Woan. A generalized measurement equation and van Cittert-Zernike theorem for wide-field radio astronomical interferometry. , 395:1558–1568, May 2009.

[20] P. M. Geil, B. M. Gaensler, and J. S. B. Wyithe. Polarized foreground removal at low radio frequencies using rotation measure synthesis: uncovering the signature of hydrogen reionization. , 418:516–535, November 2011.